Accounting for the Influence of the Tank Walls in the Zero-Sequence Topological Model of a Three-Phase, Three-Limb Transformer

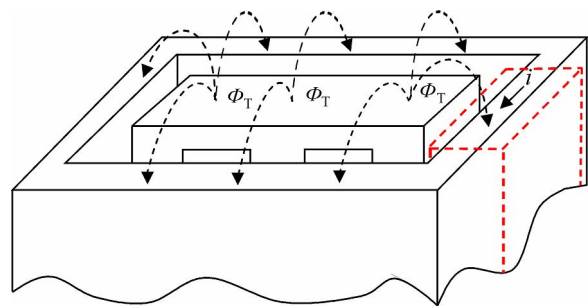Sergey E. Zirka, Yuriy I. Moroz, and Cesare M. Arturi, *Member, IEEE*

Fig. 1. Magnetodynamic model of the tank wall.

I. INTRODUCTION

ACCURATE modeling of three-limb three-phase transformers remains a challenge even when studying low-frequency transients and steady states. One reason for this is the influence of the transformer tank, which plays a two-fold role under unbalanced conditions. First, the magnetically conducting tank walls provide a path for a part of the zero-sequence magnetic flux (flux Φ_T in Fig. 1) and second, the electrically conducting walls act as a virtual winding whose current i encircles all three limbs.

The importance of taking into account the influence of the tank was pointed out in several studies [1]–[5], but no quantitative model supported by measurements has yet been developed. To investigate the impact of the tank, three major alternatives are under consideration. The first is to use simplified equivalent circuits analyzed by the method of symmetrical components [3]; the second employs topological transformer models [4], [5]; and the third involves the finite-element modeling [2], [6], which is difficult to use in transient studies. A common feature of these approaches is the solution of a linearized problem. Although linearization of the highly nonlinear system transformer

tank greatly facilitates its simulation, it is preferable to have a more comprehensive model, which could serve either as a reference for subsequent simplifications or else be used in its original form. An interesting idea of modeling the distributed nature of the core and tank was implemented in [7] where both of these elements were represented, following R. J. Meredith, by finite *LR*–sections (a type of Cauer circuit) [8]. Because of difficulties in modeling hysteresis and excess losses by means of Cauer circuits [9], we do not employ them to describe the core, preferring instead the use of a dynamic hysteresis model [9], which is a convenient tool to reproduce these loss components. However, the idea of using finite sections to model the tank inspired us to employ first, for the same purpose, the diffusion equation, which lies in the basis of constructing Cauer circuits [8]. In Section VI, we shall return to a Cauer circuit to represent the tank wall in an EMTP implementation of our model.

II. MODELING PRINCIPLE

A schematic representation of the magnetic circuit of a three-winding YNynd core-type transformer and surrounding tank walls is shown in Fig. 2, where the innermost delta-connected unloaded winding (N_3 turns per limb) plays the role of the tertiary stabilizing winding (TSW). Magnetomotive forces (MMFs) $i_1 N_1$ and $i_2 N_2$, with indices A, B, C, represent wye-connected high-voltage (HV) and low-voltage (LV) windings. The shaded elements R_L and R_Y represent the core limbs and yokes, which are described by the dynamic hysteresis model [9] Flux paths in "air" (oil) are characterized by linear reluctances shown by unshaded rectangles: R_{03} for paths between the limbs and the TSW, R_{12} for paths in the equivalent leakage channels between the HV and LV windings,

S. E. Zirka and Y. I. Moroz are with the Department of. Physics and Technology, Dnepropetrovsk National University, Ukraine 49050 (e-mail: zirka@email.dp.ua; yuriy_moroz@i.ua).

C. M. Arturi is with the Department of Electronics, Information Science, and Bioengineering, Politecnico di Milano, Milano 20133, Italy (e-mail: cesaremario.arturi@polimi.it).

Color versions of one or more of the figures in this paper are available online.
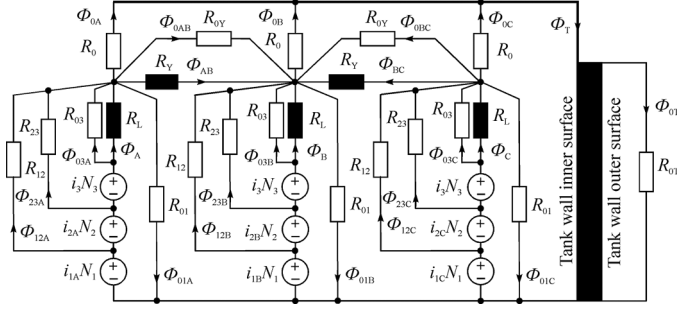
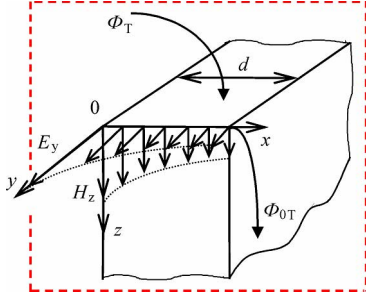Fig. 2. Magnetic network of the transformer with tank.

Fig. 3. Field distribution in the tank wall.

and R_{23} for paths between the LV winding and the TSW. The way for determining R_{12} and R_{23} is discussed in Section IV.

Reluctances R_{01} take into account the yoke-to-yoke fluxes (Φ_{01A}, Φ_{01B}, Φ_{01C}) flowing vertically between the HV windings and tank. As shown in Section IV, the shunting reluctances R_{0Y} play a role when the yokes approach saturation.

To analyze the influence of the tank wall as a surrounding winding and to avoid unnecessary complication of the transient transformer model as a network element, it is sufficient to consider the process in a central belt of the wall [10] (it is shown by the shaded four pole in Fig. 2 and partly in Figs. 1 and 3). For definiteness, the height h_T of the belt is assumed to be equal to that of the core window.

The benchmark regime for modeling the tank wall is the zero-sequence test where the three-phase terminals of the HV or LV major windings are joined at a common point and a *single-phase* voltage V is applied between this point and neutral, with the opposite winding open-circuited (LV or HV, respectively). The TSW in these tests may be either short- or open-circuited, giving the *leakage* or *magnetizing* zero-sequence impedance Z_0, respectively [1]. For both TSW connections, magnetizations of all the limbs are equal, so there are no fluxes in the yokes.

For modeling, the most stringent test is that for the open TSW when the *magnetizing* zero-sequence impedance should be reproduced. For the HV excitation, the zero-sequence magnetic fluxes leaving each limb are divided into two groups. The fluxes of the first group (yoke-to-yoke fluxes Φ_{01A}, Φ_{01B}, and Φ_{01C} in Fig. 2) are closed through the corresponding reluctances R_{01} and do not reach the tank (for this reason, these fluxes are not shown in Figs. 1 and 3).

The fluxes Φ_{0A}, Φ_{0B}, and Φ_{0C} of the second group first pass across the air gaps between the core and tank, then flow down vertically in the tank walls, and finally return to the core via

other gaps. The paths of these fluxes are represented in Fig. 2 by three linear reluctances R_0, which take into account both air gaps. As can be seen in Fig. 2, the model is not intended to detail the way in which the flux $\Phi_T (= \Phi_{0A} + \Phi_{0B} + \Phi_{0C})$ reaches the tank wall (this study requires finite-element modeling of the entire tank including its cover and bottom [6]).

It is difficult, if not impossible, to determine reluctances R_0 separately for each limb. We therefore assume them to be all equal and consider a fitting parameter of the model. The other fitting parameter is the value of the reluctances R_{01}, which are also considered equal for all three limbs despite the tank asymmetry and so there are different positions of limbs A, B, and C with respect to the tank.

To join submodels of the core and tank wall, it should be noted in Fig. 2 that fluxes Φ_{0A}, Φ_{0B}, and Φ_{0C} merge into a common flux Φ_T entering the wall.

The quantitative description of the distribution of Φ_T and i through the wall of thickness d is reduced to the integration of the 1-D Maxwell equations [11] that link the magnetic field H, the magnetic induction B, and the electric field E in a material with conductivity ó and a static hysteresis relation $B(H)$.

Using the coordinate system in Fig. 3 and z-directed vectors $H(x, t)$ and $B(x, t)$, the penetration of a plane electromagnetic wave into the wall depth is described by the partial differential equation (PDE)

$$\frac{\partial^2 H}{\partial x^2} = \sigma \frac{\partial B}{\partial t}. \tag{1}$$

To combine (1) with ordinary differential equations (ODEs) describing the lumped elements of the scheme in Fig. 2, it is convenient to introduce a uniform grid on the segment $[0, d]$ of the x-axis (see Fig. 3), with nodes x_1 at x_n at the inner and outer wall surfaces, and grid step $h = d/(n-1)$. The Neumann boundary conditions at these surfaces ($-\partial H_1/\partial x = \sigma E_1$ and $-\partial H_n/\partial x = \sigma E_n$) are determined by the values E_1 and E_n of the electric field at the first and last nodes.

Introducing grid functions $H_i(t) = H(x_i, t)$ and $B_i(t) = B(x_i, t)$ and using the approach in [11], the PDE (1) is reduced to n simultaneous ODEs

$$\frac{dB_1}{dt} = \frac{8H_2 - 7H_1 - H_3}{2\sigma h^2} + \frac{3E_1}{h},$$
$$\frac{dB_i}{dt} = \frac{H_{i-1} - 2H_i + H_{i+1}}{\sigma h^2}, (i = 2, \ldots, n-1),$$
$$\frac{dB_n}{dt} = \frac{8H_{n-1} - 7H_n - H_{n-2}}{2\sigma h^2} + \frac{3E_n}{h}. \tag{2}$$

We make a few clarifying remarks here. First, the cross-sectional area of the tank wall is always several times less than that of the core limbs. This means that the limbs remain unsaturated in zero-sequence tests, and explains why the core material has very little effect on Z_0[12]. It also causes the crucial role of the tank steel in Z_0 behavior, and, in particular, the peaked dependencies of Z_0 on the applied voltage V or current (see Fig. 9 in [13]). A suggestive observation made in [1] is that the peaked $Z_0(V)$ curve is similar to a plot of the differential permeability μ_d of the tank steel versus magnetic field H. On the other hand, a calculated graph of $\mu_d(H)$ is peaked only if the *hysteretic* properties of the steel are taken into account. In this case, the normal
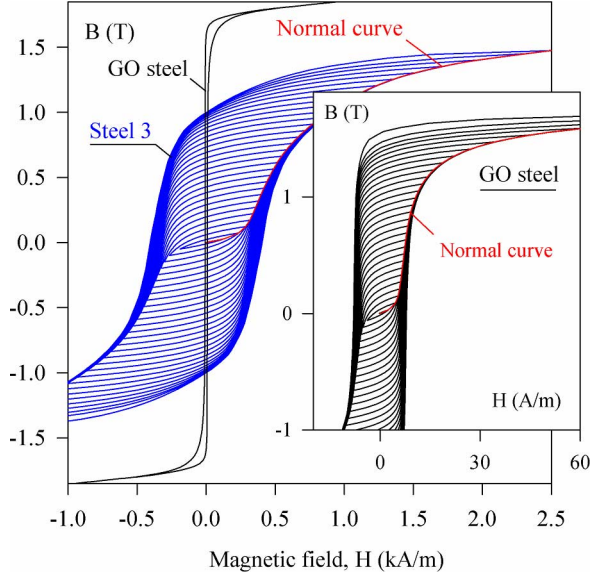
Fig. 4. Major static loops and demagnetization spirals of the GO steel of the core and the structural Steel 3 of the tank.
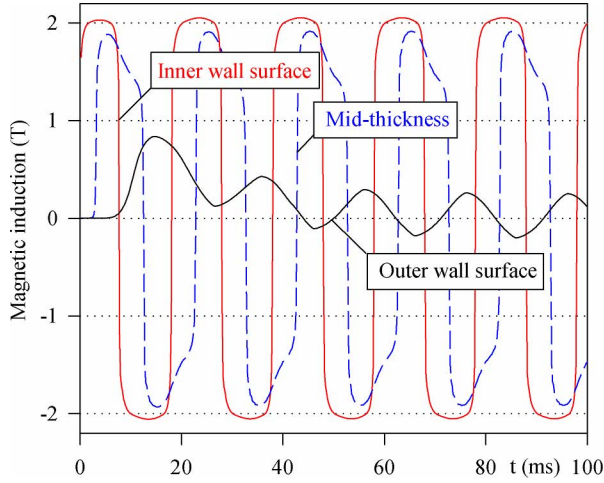

Fig. 5. Start-up transient in the wall at a terminal voltage of 40%.
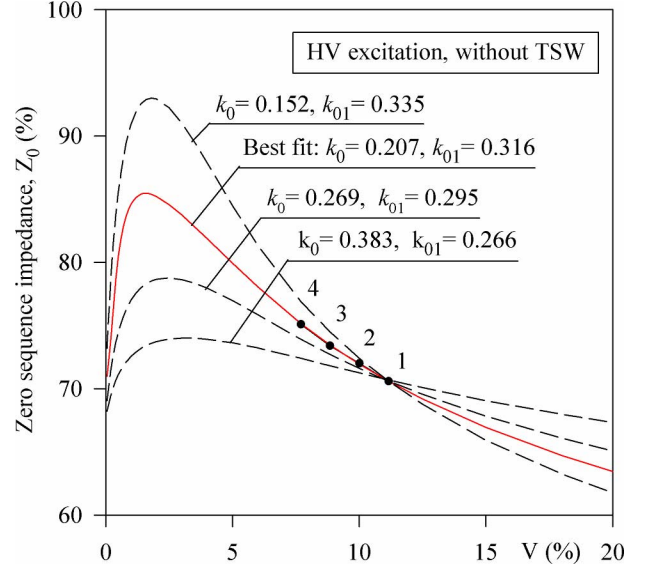

Fig. 6. Fitting the transformer model to measured values of Z_0.
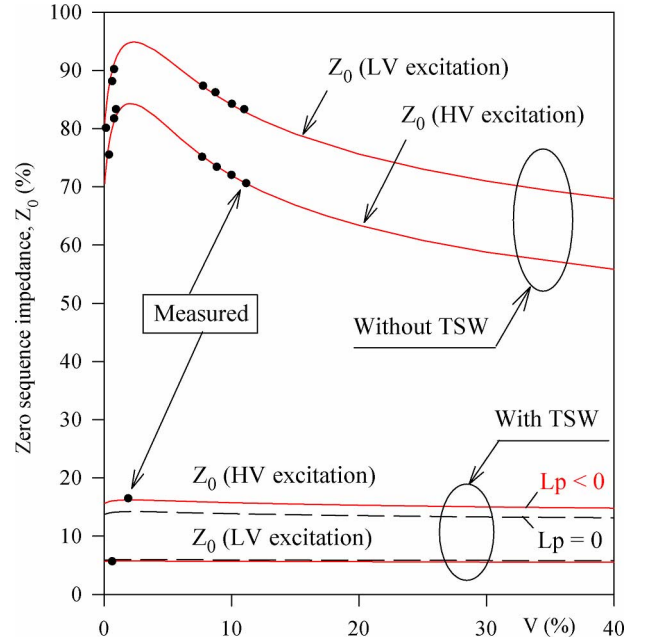
Fig. 7. Predicted Z_0 curves versus Z_0 values (dots) measured in [18].
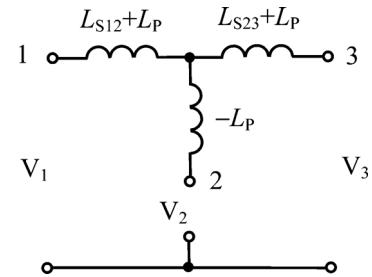
Fig. 8. Per-phase positive-sequence equivalent circuit of a three-winding transformer with dummy inductance ($-L_P$).

magnetization curve of tank Steel 3 Fig. 4 is flat at small fields, then gets steeper at moderate fields, and then again becomes flat at large fields. For this reason, H_i and B_i in (2) are related in this study through a recently proposed static hysteresis model [14].

The ODEs (2) are interrelated to the ODEs for the magnetic and electric transformer circuits using Faraday's law. For any horizontal contour lying on the inner tank surface, we can write

$$E_1 = \frac{1}{l_T} \cdot \frac{d\Phi_T}{dt} = \frac{1}{l_T} \cdot \frac{d}{dt}(\Phi_{0A} + \Phi_{0B} + \Phi_{0C}) \qquad (3)$$

where l_T is the tank perimeter, and fluxes Φ_{0A}, Φ_{0B}, Φ_{0C} are expressed by equations describing the magnetic circuit in Fig. 2. These equations are written similarly to the usage in [15].

The electric field E_n at the last node (at the outer surface of the tank wall) is given by

$$E_n = \frac{1}{l_T} \cdot \frac{d_{0T}}{dt} \qquad (4)$$

where flux Φ_{0T} leaving the tank depends on the reluctance R_{0T} of the space beyond the wall: $\Phi_{0T} = H_n(B_n)h_T/R_{0T}$. For

Fig. 9. Inrush current in phase A.

definiteness, R_{0T} is initially set equal to the reluctance of the saturated wall.

By comparing the solutions of (2) obtained for different grid spacings, we find that $n = 25$ is sufficient to obtain smooth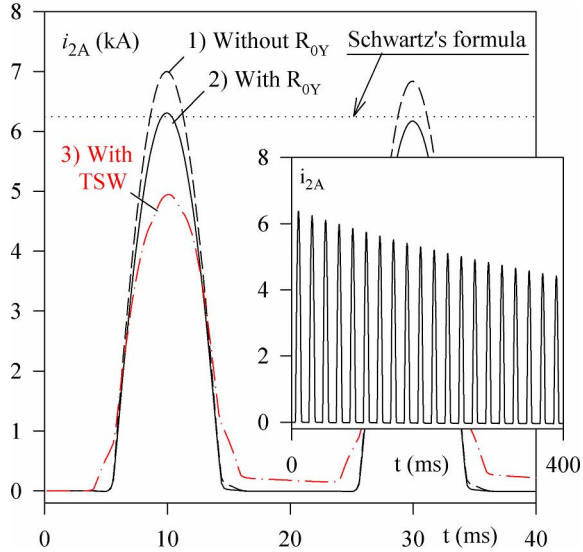 calculated curves. Together with the ODEs of the magnetic network in Fig. 2 and the ODEs of external electrical circuits, the model as a whole is described by 39 ODEs. Since these ODEs are both intricate and cumbersome, we omit them in this paper. Instead, a circuital equivalent of the model is proposed in Section VI.

III. PRELIMINARY FITTING OF THE MODEL

It is convenient to start the fit of the model to values of Z_0 measured from the HV side. In this case, the LV winding and the TSW are open-circuited, and the only MMFs in Fig. 2 are sources $i_1 N_1$. This means that shunt reluctances R_{03}, R_{23}, and R_{12} are shunted by the unsaturated limbs (the R_L elements in Fig. 2). This eliminates their influence and allows their evaluation to be postponed to Section IV.

It is difficult to find the magnetic properties of tank steel in any available sources. We were able to locate only the major hysteresis loop of structural Steel 3 [16]. It is characterized by a coercive field $H_c = 400$ A/m and resistivity $\rho = 0.14$ $\mu\Omega$·m. (Its conductivity $\sigma = 7.14 \times 10^6$ S/m is close to that in [6].)

As with any history-dependent representation of hysteresis, the model [14] used here requires well-defined initial states for the core and tank. To define these states, the calculation begins by modeling the demagnetization procedures for both tank and core steels. Modeled demagnetization spirals of the structural Steel 3 used for the tank and the grain-oriented (GO) steel of the core are shown in Fig. 4.

The turning points and reversal curves of the procedures are copied into the memory for each node of the wall grid and core branches (limbs and yokes), and then updated independently for every element during the transient calculation.

If the properly-demagnetized material is magnetized in, say, the "positive" direction and if the history-dependent hysteresis

model is used, then the $B - H$ curve in the first quadrant will pass successively through all of the turning points of the demagnetizing spiral. The *normal* curves obtained in this way for both steels are included in Fig. 4.

When modeling the zero-sequence test, a single-phase terminal voltage is applied to the transformer. To short the transient and obtain symmetrical flux densities in the core and tank, this sinusoidal voltage V should reach its maximum at the time of application. Then three to five periods are usually sufficient to reach a steady-state flux in the wall depth. This can be seen in Fig. 5, which shows flux densities at both surfaces of the modeled wall (B_1 and B_{25}) and at its mid-thickness (B_{13}). When the transient in the wall is complete, the zero-sequence transformer impedance Z_0 is calculated in percent in accordance with the IEEE Standard [17].

The fitting of the model to experimental data is illustrated in Fig. 6 where points 1 to 4 represent the values of the zero-sequence magnetizing impedance measured at different voltages (in percent to the rated phase voltage) on the HV side of a 25-MVA transformer [18].

The fitting parameters that are employed (R_0 and R_{01}) can be characterized by the ratios $k_0 = R_0/R_{12}$ and $k_{01} = R_{01}/R_{12}$. It can be seen in Fig. 6 that any number of pairs of k_0 and k_{01} can guarantee that the calculated Z_0-versus-voltage curve passes through measured point 1. However, only one $k_0 - k_{01}$ pair can ensure that this curve will pass through all four measured points and thereby adjust the model.

The predictive abilities of the adjusted model can be seen in Fig. 7 where Z_0 curves calculated with and without the TSW agree very closely with Z_0 values obtained in experiment [18] for HV and LV excitations.

Although a decrease of Z_0 in the presence of TSW is a well-known effect, we see a small variation of Z_0 even in this case. It is also interesting and apparently paradoxical that the flux distribution shown in Fig. 5 takes place during the absence and presence of the TSW.

It is observed at this stage that the Z_0 values are insensitive to R_{0T}. A two-order decrease in R_{0T} has no effect on Z_0 at V < 0.6 p.u., and results in less than a 2% decrease in Z_0 at V = 1 p.u. at the open TSW.

IV. MODELING FLUX LEAKAGE

In any transformer with three concentric windings (1, 2, 3) and binary short-circuit inductances L_{S12}, L_{S23}, L_{S13}, referred to as a common number of turns (say N_2), there is an inequality $L_{S13} > L_{S12} + L_{S23}$ because of the finite thicknesses of the middle winding 2 [19]. To satisfy this inequality, two equivalent methods can be employed. The first (used in the present model) is to use additional inductances L_p in the per-phase positive-sequence circuit in Fig. 8[4], while the second is the introduction of magnetic coupling between inductances L_{S12} and L_{S23} in its horizontal branches [19].

The positive-sequence equivalent circuit [4] contains a positive inductance L_P in both the horizontal branches, and a negative inductance $-L_P$ in the vertical branch. This is shown in Fig. 8, where the large magnetization inductances of the unsaturated core and the small winding resistances are omitted for clarity.

As can be seen in Fig. 8 and in the circuital (dual) scheme developed in Section VI, the negative inductance $-L_{\mathrm{p}}$ is *always* in series with the positive inductance $+L_{\mathrm{p}}$. So the resulting inductance of any path including $-L_{\mathrm{p}}$ is positive. This explains the stability of the model.

It is obvious that the circuit in Fig. 8 matches all terminal inductances $L_{\mathrm{S}12}$, $L_{\mathrm{S}23}$, $L_{\mathrm{S}13}$ if

$$L_{\mathrm{p}} = \frac{L_{\mathrm{S}13} - (L_{\mathrm{S}12} + L_{\mathrm{S}23})}{2}. \qquad (5)$$

After calculating L_{p}, the leakage reluctances in Fig. 2 are found as $R_{12} = N_2^2/(L_{\mathrm{S}12} + L_{\mathrm{P}})$ and $R_{23} = N_2^2/(L_{\mathrm{S}23} + L_{\mathrm{P}})$. The negative inductances $-L_{\mathrm{P}}$ can be represented in Fig. 2 by the negative reluctances $R_{\mathrm{p}} = N_2^2/(-L_{\mathrm{P}})$ in parallel with the MMF sources $i_{2\mathrm{A}}N_2$, $i_{2\mathrm{B}}N_2$, and $i_{2\mathrm{C}}N_2$[4]. As an alternative (employed in the present model), these inductances $(-L_{\mathrm{p}})$ are used as elements of the *electrical* circuit (not shown in Fig. 2) where they are included in series with the middle (LV) windings.

The linear reluctance R_{03} in the network in Fig. 2 characterizes the gap between the innermost winding (TSW) and the core. It can be noted that R_{03} (and corresponding inductance) is not a "leakage" element and cannot be measured directly. For this reason, we can set it equal to $2R_{23}$[20]. This means that the reactance $X_{03} = \omega N_2^2/R_{03}$ of the innermost channel and the reactance $X_{23} = \omega N_2^2/R_{23}$ of the nearest leakage channel are linked by the factor $k = X_{03}/X_{23} = R_{23}/R_{03} = 0.5$ as was postulated in [20] and then employed in some other studies.

The only model parameter remaining to be described at this point is the value of the air (linear) reluctances $R_{0\mathrm{Y}}$ in parallel with the yokes. To choose $R_{0\mathrm{Y}}$, the aforementioned regime can be considered. This is the case when the ideal source of the three-phase voltage is connected to the LV windings with other windings kept open-circuited (at the open TSW, $L_{\mathrm{p}} = 0$ in all of the previous formulas).

For definiteness, let the voltage of phase A cross zero at $t = 0$. Then, the inrush current in phase A is the highest, and only this current $i_{2\mathrm{A}}$ is considered in this section. Since no information about the inrush current properties of this transformer is given in [18], we can evaluate $R_{0\mathrm{Y}}$ by using only indirect considerations.

The first numerical experiment was to calculate startup transients in the absence of $R_{0\mathrm{Y}}$. The corresponding current is shown in Fig. 9 by the dashed curve 1. Fig. 10 shows flux densities in the lateral limb A (bearing the winding A) and in the yoke AB adjacent to this limb. Although curve 1 in Fig. 10 is correct in the sense that the flux-density peak B_{Ym} in the yoke is always less than that in the limb, an obviously overestimated B_{Ym} is observed in the model *without* $R_{0\mathrm{Y}}$. Its value ($B_{\mathrm{Ym}} = 2.134$ T) is markedly higher than that ($B = 2.025$ T) at which the steel employed reaches technical saturation [15]. So in the absence of $R_{0\mathrm{Y}}$, the following nonphysical situation occurs when the yoke is heavily saturated: there is a high flux density in the yoke (characterized by the differential permeability μ_0), but there is *no* magnetic flux surrounding the medium with the same permeability μ_0.

This contradiction can be eliminated by introducing reluctances $R_{0\mathrm{Y}}$ which allow the flux to be divided between the yoke itself and the space beyond the yoke. It is convenient to relate the value of $R_{0\mathrm{Y}}$ to the reluctance of the saturated yoke R_{YS}. It was
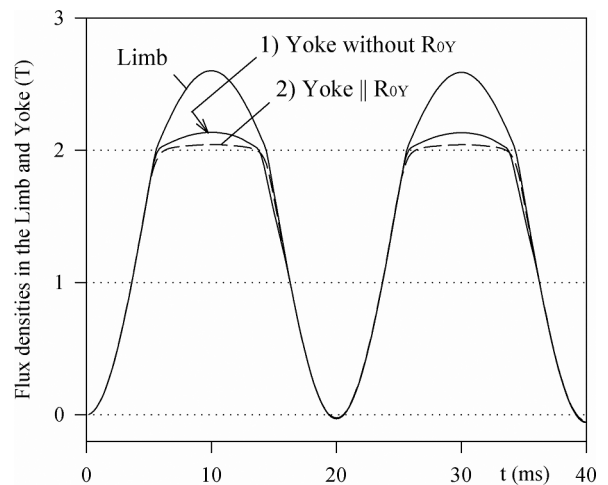

Fig. 10. Flux densities in the limb "A" and the adjacent yoke.

found numerically that at $R_{0\mathrm{Y}}/R_{\mathrm{YS}} = 0.08$, the first current peak (solid curve 2 in Fig. 9) is consistent with that calculated with Schwartz's formula [15] (it is shown as the dotted horizontal). At such an $R_{0\mathrm{Y}}$, the flux density in the saturated yoke does not exceed 2.041 T (curve 2 in Fig. 10), and the flux in $R_{0\mathrm{Y}}$ is about half of that in the yoke. The inset of Fig. 9 shows the decay of inrush current and illustrates the stability of the model over the long term.

To complete the theme of inrush currents, we note that the current calculated in the presence of the TSW (curve 3 in Fig. 9) has markedly lower peaks than those calculated with the open-circuited TSW.

V. PROCESSES IN THE CENTRAL BELT OF THE TANK WALL

The measurements and calculations in Fig. 7, carried out for the open TSW, illustrate a strong dependence of Z_0 on the applied voltage. This raises a question about the reliability of results obtained with linearized tank models.

The first peculiarity to be investigated is the skin effect in the magnetically nonlinear tank material. It is worthwhile to note in Fig. 5 that peak flux densities at the mid-thickness of the wall and its inner surface are not too different (at $V = 40\%$), contradicting the behavior predicted by the linear theory. The reason is the saturable character of the $B(H)$ dependence of the tank steel. As the surface layers approach saturation, their reluctances increase resulting in the displacement of the magnetic flux into the depth of the wall. This leads to a leveling of the peak flux densities over the wall cross section. Fig. 11 depicts the maximum induction values over the tank wall thickness calculated for a wide range of the terminal voltages during the zero-sequence tests. At voltages below several percent, a typical skin effect is observed, that is, there is no magnetic flux in the middle of the wall. As the voltage increases, the flux distribution becomes more uniform, as described before.

Regarding the similarity between the peaked curves in Fig. 7 and the graph of the differential permeability of the tank steel versus magnetic field [1], we see this resemblance to be qualitative rather than quantitative. Since the curves in Fig. 7 are functions of voltage (not of the field), the terminal voltage is used as the variable parameter in the subsequent analysis. Fig. 12 shows
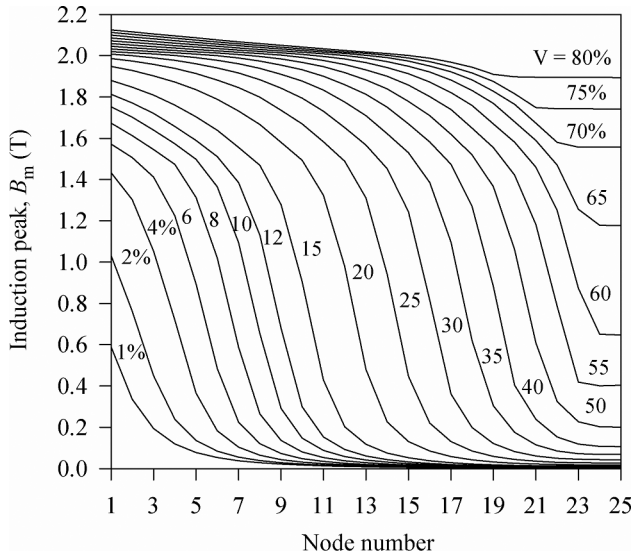
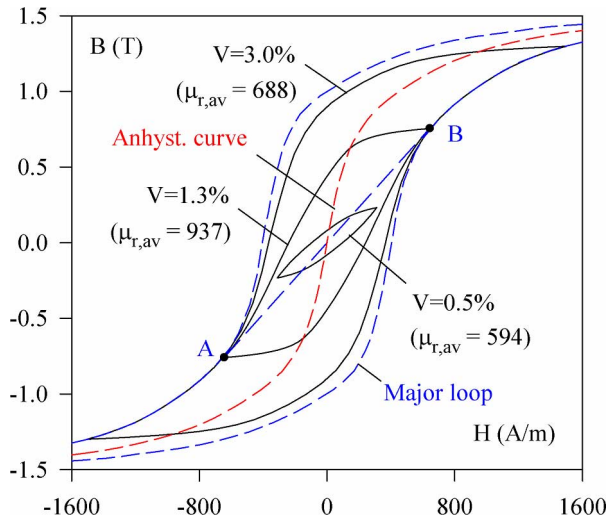Fig. 11. Flux-density profiles over the tank wall thickness.

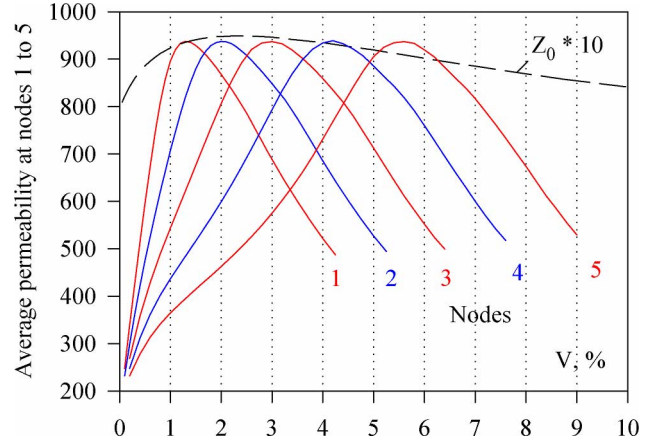Fig. 12. Hysteresis loops at the inner surface of the tank wall.

Fig. 13. Average permeabilities in the first five nodes versus terminal voltage.

Fig. 14. Zero-sequence flux Φ_0 and its components Φ_{01} and Φ_T .

steady-state hysteresis loops at the inner surface of the wall calculated at the per-unit voltages of 0.5, 1.3, and 3%. Since the differential permeability changes by orders of magnitude during the cycle, its average value was used to characterize a loop. It is determined by the tangent of the slope of the straight line connecting the loop tips. The line A-B in Fig. 12 is drawn for the loop obtained at V = 1.3%, which has the highest slope among all loops of the surface node 1, that is., the highest average relative permeability $\mu_{r,av} = 937$.

The plots of $\mu_{r,av}$ calculated for the first five nodes of the 25-node wall grid are shown in Fig. 13. For comparison, the highest Z_0-curve of Fig. 7 is also shown in Fig. 13. It is properly rescaled (multiplied by 10) for comparison with the $\mu_{r,a}(V)$ profiles.

It is seen in Fig. 13 that the $Z_0(V)$ curve reaches its maximum when the average permeabilities in the first three nodes are also near their maxima. In this context, it is instructive to analyze the distribution of the zero-sequence flux Φ_0 between the tank (flux Φ_T in Fig. 2) and the direct air paths from yoke to yoke

(flux $\Phi_{01} = \Phi_{01A} + \Phi_{01B} + \Phi_{01C}$). The maximum values of flux Φ_0 and its components Φ_T and Φ_{01}, calculated at the HV excitation, are shown in Fig. 14. Because of the phase shift between Φ_T and $\Phi_{01,}$ and owing to the nonsinusoidal waveform of Φ_T, the maximum of Φ_0 is not equal to the sum of maxima of Φ_T and Φ_{01}. Also, a small flux Φ_{0T} appears beyond the tank at large voltages.

It is remarkable in Fig. 14 that, at voltages less than 7%, flux Φ_T in the tank is somewhat higher than that (Φ_{01}) from yoke to yoke. So the role of the tank as a magnetically conducting element dominates at low voltages. As the voltage increases, more deep "layers" of the tank reach saturation and its reluctance increases. At the same time, the penetration of the flux into the wall induces eddy currents in its deeper layers requiring additional current from the voltage source to overcome their demagnetizing effect. The rise of the source current manifests itself in decreasing Z_0.

The conventional boundary between the tank permeance and the tank conductor (virtual winding) is seen as the peaks in Z_0 curves in Fig. 7 calculated without the TSW. The calculations
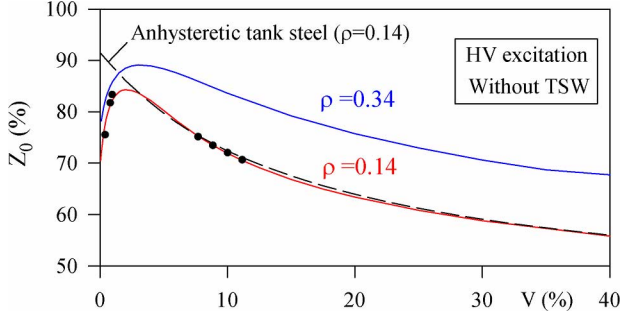
Fig. 15. Influence of the resistivity and hysteresis of the tank material on the zero-sequence impedance.

represented in Fig. 15 show that when the tank is made of *alloyed* steel ($\rho = 0.34$ $\mu\Omega\cdot$m), this boundary is shifted to higher voltages, and the values of Z_0 are increased.

Finally, considering the average permeabilities of the various minor loops in Fig. 12, it is expected that the peaks of the Z_0 curves in Fig. 7 can only be reproduced if the hysteretic properties of the tank material are taken into account. If the anhysteretic curve of the tank steel is employed instead of the hysteresis model (this curve can be constructed by a "horizontal" averaging of the major loop branches), the model predicts a monotonically falling Z_0 curve, as shown by the dashed line in Fig. 15. On the other hand, Fig. 15 shows that Z_0 curves calculated using both the hysteretic and anhysteretic tank models practically coincide at voltages exceeding 5%.

VI. MODELING IN EMTP–ATP

By means of the widely used duality transformation and the approach proposed in [21], the circuital equivalent of the magnetic model in Fig. 2 can be shown as depicted in Fig. 16, where the linear inductances ($L = N_2^2/R$) are determined by the corresponding reluctances R in Fig. 2. Nine ideal transformers (IT) serve to relate the model parameters to the number of turns N_2 of the LV (intermediate) winding.

The five dynamic-hysteresis-model (DHM) elements are EMTP-ATP implementations of the DHM [9], which consists of a static hysteresis model [14] and dynamic components that describe classical and excess losses in the core limbs and yokes [9]. (Details of the DHM implementation in ATP will be published elsewhere.)

When the switch S is open, resistor $R = 10^9$ Ω makes the TSW nonconducting, and the transformer becomes two winding. The three grounding resistors $R(= 10^9 \ \Omega)$ provide a means to eliminate the effect of the floating subnetwork of the TSW. Resistors r_1, r_2, and r_3 are winding resistances. The tank wall is represented in Fig. 16 by a ladder circuit (LC) consisting of 24 T-sections, corresponding to $n = 25$ (see Section II). The LC resistors are calculated from $R = N_2^2 \rho \, l_T/(h_T h)$.

Since a nonhysteresis tank representation can be used to model this transformer at $V > 5\%$, the anhysteretic curve $B(H)$ of the tank steel is used in this section. This curve is transformed into the flux linkage (λ) versus current (i) curve of the nonlinear inductances of the LC using the relationships $\lambda = B \cdot l_T N_2 h$ and $i = H \cdot h_T/N_2$. The latter formula can also
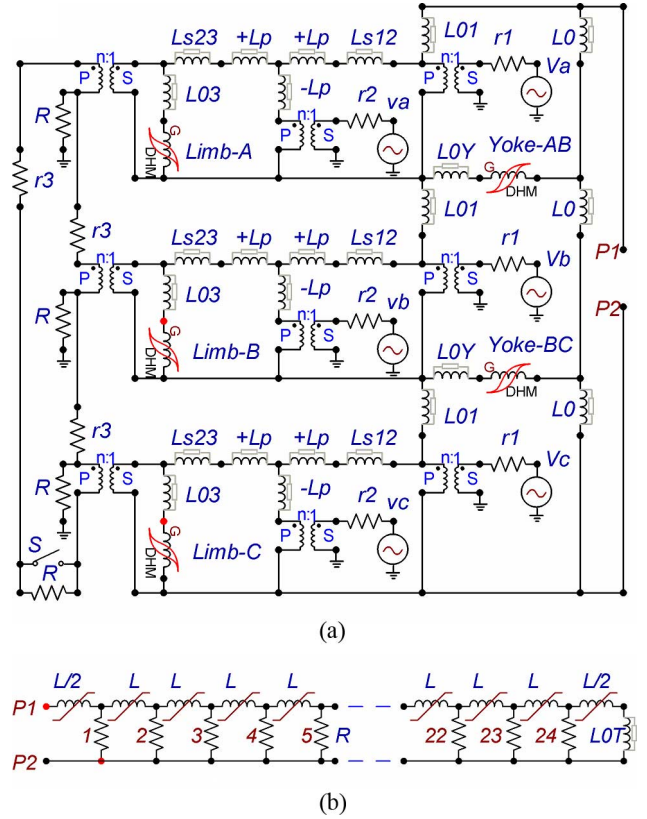

(a)

(b)

Fig. 16. (a) Equivalent electric circuit of a three-limb transformer. (b) Tank wall model connected through terminals P1-P2.
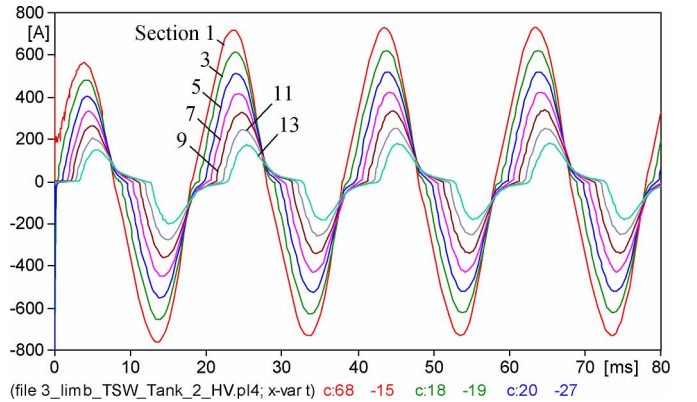

Fig. 17. Currents (fields) in sections 1, 3, 5, 7, 9, 11, and 13 of the ladder circuit.

be used to recalculate the LC currents to give the magnetic-field values for corresponding "layers" of the tank wall.

The currents in the first few odd-order cells of the LC are shown in Fig. 17. Similar to the induction profiles in Fig. 5, these currents were calculated for $V = 40\%$. This was done to show the different manifestations of the skin effect with respect to the induction and field in the tank wall. Although the field amplitudes decrease rapidly with depth (Fig. 17), they remain large enough to maintain saturation in the inner layers of the wall (Fig. 5). The results obtained with the circuital model of Fig. 16 were verified by calculations for the magnetic network that is employed here as a reference model. If the transformer

capacitances are significant, they can be included in the afore-mentioned inductive models, as in [5].

VII. Conclusion

This paper proposes a new conceptual model of a three-phase three-limb core-type transformer. It shows that the electrically and magnetically conducting tank walls play the roles of a magnetic shunt and a virtual winding. It is shown that peaked Z_0-versus-voltage curves can be reproduced only when the hysteretic properties of the tank steel are taken into account. The fitting of the model is achieved by properly dividing the zero-sequence magnetic flux between the flux in the tank walls and the yoke-to-yoke flux in air.

Postponing technical applications of the model to future publications, we note that it provides reliable explanations of the transformer behavior under transient and steady-state conditions. The model allows one to observe phenomena that are difficult to predict using simple linear approaches and theories. Among its other attributes, this makes the model an appropriate tool for evaluating the role of the tertiary stabilizing winding in three-phase Y-Y-connected power transformers.

References

[1] S. V. Kulkarni and S. A. Khaparde, *Transformer Engineering: Design and Practice*.   New York: Marcel Dekker, 2004.

[2] T. Ngnegueu, M. Mailhot, A. Munar, and M. Sacotte, "Zero phase sequence impedance and tank heating model for three phase three leg core type power transformers coupling magnetic field and electric circuit equations in a finite element software," *IEEE Trans. Magn.*, vol. 31, no. 3, pp. 2068–2071, May 1995.

[3] P. Penabad-Duran, X. M. Lopez-Fernandez, and C. Alvarez-Marino, "Transformer tertiary stabilizing windings. Part I: apparent power rating," in *Proc. XXth Int. Conf. El. Mach.*, Marseille, France, Sep. 2012, pp. 2362–2368.

[4] X. Chen and S. S. Venkata, "A three-phase three-winding core-type transformer model for low-frequency transient studies," *IEEE Trans. Power Del.*, vol. 12, no. 2, pp. 775–782, Apr. 1997.

[5] J. A. Martinez, R. Walling, B. A. Mork, J. Martin-Arnedo, and D. Durbak, "Parameter determination for modeling system transients-Part III: Transformers," *IEEE Trans. Power Del.*, vol. 20, no. 3, pp. 2051–2062, Jul. 2005.

[6] P. Penabad-Duran, C. Alvarez-Marino, and X. M. Lopez-Fernandez, "Transformer tertiary stabilizing windings. Part II: Overheating hazard on tank walls," in *Proc. XXth Int. Conf. El. Mach.*, Marseille, France, 2012, pp. 2369–2374.

[7] L. Colla, V. Iuliani, F. Palone, M. Rebolini, and C. Taricone, "EHV/HV autotransformers modeling for electromagnetic transients simulation of power systems," in *Proc. XIXth Int. Conf. El. Mach.*, Rome, Italy, 2010, pp. 2453–2458.

[8] E. A. Boldirev, M. X. Zicherman, and N. P. Kameneva, "Alternative electromagnetic field in conducting sheet with nonlinear magnetic permeability," (in Russian) *Elektrichestvo*, no. 3, pp. 61–67, 1974.

[9] S. E. Zirka, Y. I. Moroz, A. J. Moses, and C. M. Arturi, "Static and dynamic hysteresis models for studying transformer transients," *IEEE Trans. Power Del.*, vol. 26, no. 4, pp. 2352–2362, Oct. 2011.

[10] N. D. Tleis, *Power Systems Modelling and Fault Analysis: Theory and Practice*.   New York: Newnes/Elsevier, 2008.

[11] S. E. Zirka, Y. I. Moroz, P. Marketos, and A. J. Moses, "Viscosity-based magnetodynamic model of soft magnetic materials," *IEEE Trans. Magn.*, vol. 42, no. 9, pp. 2121–2132, Sep. 2006.

[12] G. R. Slemon, "Equivalent circuits for transformers and machines, including non-linear effects," *Proc. Inst. Elect. Eng.*, vol. 100, no. 5, pp. 129–143, 1953.

[13] *Power Transformers — Application Guide. Ed. 1997–10*, Int. Std. IEC 60076–8, 1997.

[14] S. E. Zirka, Y. I. Moroz, R. G. Harrison, and N. Chiesa, "Inverse hysteresis models for transient simulation," *IEEE Trans. Power Del.*, vol. 29, 2014, to be published.

[15] S. E. Zirka, Y. I. Moroz, C. M. Arturi, N. Chiesa, and H. K. Høidalen, "Topology-correct reversible transformer model," *IEEE Trans. Power Del.*, vol. 27, no. 4, pp. 2037–2045, Oct. 2012.

[16] A. N. Kravchenko and L. P. Nizhnik, *Electrodynamic Computations in Electrical Engineering.* (in Russian).   Kiev, Ukraine: Technika, 1977.

[17] *IEEE Standard Test Code for Liquid-Immersed Distribution, Power and Regulating Transformers*, IEEE Standard C57.12.90, 2010.

[18] A. Ramos, J. C. Burgos, A. Moreno, and E. Sorrentino, "Determination of parameters of zero-sequence equivalent circuits for three-phase three-legged YNynd transformers based on onsite low-voltage tests," *IEEE Trans. Power Del.*, vol. 28, no. 3, pp. 1618–1625, Jul. 2013.

[19] F. DeLeon and J. A. Martinez, "Dual three-winding transformer equivalent circuit matching leakage measurements," *IEEE Trans. Power Del.*, vol. 24, no. 1, pp. 160–168, Jan. 2009.

[20] B. A. Mork, F. Gonzalez, and D. Ishchenko, "Leakage inductance model for autotransformer transient simulation," presented at the Int. Conf. Power Syst. Transients, Montreal, QC, Canada, 2005.

[21] C. M. Arturi, "Transient simulation of a three phase five limb step-up transformer following an out-of-phase synchronization," *IEEE Trans. Power Del.*, vol. 6, no. 1, pp. 196–207, Jan. 1991.